Large Binocular Telescope Search for Companions and Substructures in the (Pre)transitional Disk of AB Aurigae

Sebastián Jorquera, Mickaël Bonnefoy, Sarah Betti, Gaël Chauvin, Esther Buenzli, Laura M. Pérez, Katherine B. Follette, Philip M. Hinz, Anthony Boccaletti, Vanessa Bailey, et al.

▶ **To cite this version:**

Sebastián Jorquera, Mickaël Bonnefoy, Sarah Betti, Gaël Chauvin, Esther Buenzli, et al.. Large Binocular Telescope Search for Companions and Substructures in the (Pre)transitional Disk of AB Aurigae. The Astrophysical Journal, 2022, 926, 10.3847/1538-4357/ac4be4 . insu-03636653

HAL Id: insu-03636653
https://insu.hal.science/insu-03636653

Submitted on 20 Jun 2022

HAL is a multi-disciplinary open access archive for the deposit and dissemination of scientific research documents, whether they are published or not. The documents may come from teaching and research institutions in France or abroad, or from public or private research centers.

L'archive ouverte pluridisciplinaire **HAL**, est destinée au dépôt et à la diffusion de documents scientifiques de niveau recherche, publiés ou non, émanant des établissements d'enseignement et de recherche français ou étrangers, des laboratoires publics ou privés.

Distributed under a Creative Commons Attribution 4.0 International License

The Astrophysical Journal, 926:71 (9pp), 2022 February 10 https://doi.org/10.3847/1538-4357/ac4be4
© 2022. The Author(s). Published by the American Astronomical Society.
OPEN ACCESS

Large Binocular Telescope Search for Companions and Substructures in the (Pre) transitional Disk of AB Aurigae

Sebastián Jorquera[1,2], Mickaël Bonnefoy[2,3], Sarah Betti[4], Gaël Chauvin[2,5], Esther Buenzli[3], Laura M. Pérez[1,6], Katherine B. Follette[7], Philip M. Hinz[8], Anthony Boccaletti[9], Vanessa Bailey[10], Beth Biller[3,11,12], Denis Defrère[13], Josh Eisner[14], Thomas Henning[3], Hubert Klahr[3], Jarron Leisenring[14], Johan Olofsson[3,15,16], Joshua E. Schlieder[3,17], Andrew J. Skemer[8], Michael F. Skrutskie[18], and Roy Van Boekel[3]

[1] Departamento de Astronomía, Universidad de Chile, Camino El Observatorio 1515, Las Condes, Santiago, Chile
[2] Université Grenoble Alpes, CNRS, IPAG, F-38000 Grenoble, France
[3] Max-Planck-Institut für Astronomie, Königstuhl 17, D-69117 Heidelberg, Germany
[4] Department of Astronomy, University of Massachusetts, Amherst, MA 01003, USA
[5] Unidad Mixta Internacional Franco-Chilena de Astronomía, CNRS/INSU UMI 3386, France
[6] Núcleo Milenio de Formación Planetaria (NPF), Chile
[7] Physics & Astronomy Department, Amherst College, 21 Merrill Science Dr., Amherst, MA 01002, USA
[8] Department of Astronomy and Astrophysics, University of California, Santa Cruz, 1156 High St, Santa Cruz, CA 95064, USA
[9] LESIA, Observatoire de Paris, Université PSL, CNRS, Sorbonne Université, Univ. Paris Diderot, Sorbonne Paris Cité, 5 place Jules Janssen, F-92195 Meudon, France
[10] Jet Propulsion Laboratory, California Institute of Technology, Pasadena, CA 91109, USA
[11] SUPA, Institute for Astronomy, University of Edinburgh, Blackford Hill, Edinburgh EH9 3HJ, UK
[12] Centre for Exoplanet Science, University of Edinburgh, Edinburgh, UK
[13] Institute of Astronomy, KU Leuven, Celestijnlaan 200D, B-3001 Leuven, Belgium
[14] Steward Observatory, University of Arizona, 933 North Cherry Ave. Tucson, AZ 85721, USA
[15] Instituto de Física y Astronomía, Facultad de Ciencias, Universidad de Valparaíso, Av. Gran Bretaña 1111, Playa Ancha, Valparaíso, Chile
[16] Núcleo Milenio Formación Planetaria—NPF, Universidad de Valparaíso, Av. Gran Bretaña 1111, Valparaíso, Chile
[17] Exoplanets and Stellar Astrophysics Laboratory, Code 667, NASA Goddard Space Flight Center, Greenbelt, MD, 20771, USA
[18] Department of Astronomy, University of Virginia, Charlottesville, VA 22904, USA
Received 2021 October 13; revised 2022 January 10; accepted 2022 January 15; published 2022 February 15

Abstract

Multiwavelength high-resolution imaging of protoplanetary disks has revealed the presence of multiple, varied substructures in their dust and gas components, which might be signposts of young, forming planetary systems. AB Aurigae bears an emblematic (pre)transitional disk showing spiral structures observed in the inner cavity of the disk in both the submillimeter (Atacama Large Millimeter/submillimeter Array (ALMA); 1.3 mm, ^{12}CO) and near-infrared (Spectro-polarimetric High-contrast Exoplanet Research; 1.5–2.5 μm) wavelengths, which have been claimed to arise from dynamical interactions with a massive companion. In this work, we present new deep K_s (2.16 μm) and L' (3.7 μm) band images of AB Aurigae obtained with the L/M-band Infrared Camera on the Large Binocular Telescope, aimed for the detection of both planetary companions and extended disk structures. No point source is recovered, in particular at the outer regions of the disk, where a putative candidate ($\rho = 0\farcs681$, PA $= 7\fdg6$) had been previously claimed. The nature of a second innermost planet candidate ($\rho = 0\farcs16$, PA $= 203\fdg9$) cannot be investigated by the new data. We are able to derive 5σ detection limits in both magnitude and mass for the system, going from 14 $M_{\rm Jup}$ at $0\farcs3$ (49 au) down to 3–4 $M_{\rm Jup}$ at $0\farcs6$ (98 au) and beyond, based on the ATMO 2020 evolutionary models. We detect the inner spiral structures ($<0\farcs5$) resolved in both CO and polarimetric H-band observations. We also recover the ring structure of the system at larger separation ($0\farcs5$–$0\farcs7$) showing a clear southeast/northwest asymmetry. This structure, observed for the first time at L' band, remains interior to the dust cavity seen at ALMA, suggesting an efficient dust trapping mechanism at play in the disk.

Unified Astronomy Thesaurus concepts: Protoplanetary disks (130); Direct imaging (387); Exoplanets (498); Exoplanet astronomy (486)

1. Introduction

The high-resolution capabilities of Spectro-polarimetric High-contrast Exoplanet Research (ALMA; e.g., ALMA Partnership et al. 2015; Andrews et al. 2018; Pérez et al. 2020) in thermal imaging and of ground-based extreme-AO imager instruments in scattered light, e.g., Spectro-polarimetric High-contrast Exoplanet Research (SPHERE; Benisty et al. 2015; Stolker et al. 2016; Avenhaus et al. 2018), Subaru Coronagraphic Extreme Adaptive Optics (SCExAO; Uyama et al. 2020), Large Binocular Telescope Interferometer (LBTI; Wagner et al. 2020), have dramatically refined our view of circumstellar disks, revealing substructures in their dust and gas distribution (spirals, concentric annuli, large-scale asymmetries, broken arcs, etc.), and providing direct (Keppler et al. 2018; Benisty et al. 2021) or indirect (Pinte et al. 2019, 2020) evidence of forming planets embedded in these disks.

In this context, the Herbig Ae star AB Aurigae ($d = 162.9 \pm 15$ pc, Gaia Collaboration et al. 2018; $M = 2.4 \pm 0.2\,M_\odot$, DeWarf et al. 2003) stands out as one of the most extensively studied young star to date, and a prime example of the complementarity between near-infrared (NIR) and submillimeter studies. Polarized light images of the disk in the NIR (Fukagawa et al. 2004;

Original content from this work may be used under the terms of the Creative Commons Attribution 4.0 licence. Any further distribution of this work must maintain attribution to the author(s) and the title of the work, journal citation and DOI.

Table 1
Observing Log

Date	Time (UT)	Target	Tel. eye	Band	# exp.	Used # exp.	θ (°)	Seeing (″)	Data Set
2014 02 09	02:28–03:58	AB Aur	SX	L'	2700	2052	−69/76	0.71–1.06	1
2014 02 13	02:19–03:39	AB Aur	DX	L'	2015	1515	−66/76	0.66–1.05	2
2014 02 13	02:19–03:39	AB Aur	SX	L'	2015	1558	−66/76[a]	0.66–1.05	3
2014 02 13	04:04–04:35	HD39925	DX	L'	1210	1098	62/75	0.73–1.42	ref2
2014 02 13	04:04–04:35	HD39925	SX	L'	1210	1077	62/75	0.73–1.42	ref3
2014 02 13	04:46–06:53	AB Aur	DX	L'	2500	1240	77/70	0.68–1.41	4
2014 02 13	04:46–06:53	AB Aur	SX	L'	2500	1990	77/70	0.68–1.41	5
2014 02 13	07:06–07:31	HD39925	DX	L'	1020	640	73/72	1.02–1.83	ref4
2014 02 13	07:06–07:31	HD39925	SX	L'	1020	878	73/72	1.02–1.83	ref5
2015 01 04	04:08–04:26	HIP22138	SX	K_s	480	424	−70/−65	0.74–1.03	ref6
2015 01 04	04:42–04:59	AB Aur	SX	K_s	480	430	−74/−65	0.76–1.19	6
2015 01 04	05:23–05:40	AB Aur	SX	K_s	480	414	2/60	unk—3.18	7
2015 01 04	07:13–07:30	HIP24447	SX	K_s	480	402	79/80	0.68–0.76	ref7

Note.
[a] AO loop was open for parallactic angles θ from −61° to 54°.

Perrin et al. 2009) have revealed multiple spiral structures in the outer regions of the system, extending up to 450 au, together with a warped double ring structure (inner ring radius of 92 au, outer ring radius of 210 au) separated by a gap located at ≈170 au (Hashimoto et al. 2011). Millimeter-wave observations allowed the detection of a large disk in CO, with a central cavity in the dust of 70 au radius (Piétu et al. 2005). Additionally, Tang et al. (2012) found counterrotating CO spirals at the outer regions of the disk, with two of them having counterparts in the NIR.

More recent millimeter and NIR high-angular-resolution campaigns resolved the innermost regions of AB Aur. Using ALMA, Tang et al. (2017) identified a dust ring with a radius of ≈120 au, together with the detection of two clearly defined CO spirals inside the disk cavity, apparently linked to the presence of one or more unseen planetary companions. Following the ALMA observations, Boccaletti et al. (2020) performed H-band (1.625 μm) and K-band (2.182 μm) polarimetric and angular differential imaging (hereafter, ADI) observations of AB Aur with SPHERE at the Very Large Telescope (VLT) and reported the detection of two spiral structures inside the disk cavity, together with two apparent point sources at ≈30 au and ≈110 au. The presence of companions on the system had already been previously discussed based on indirect signatures (Millan-Gabet et al. 2006; Oppenheimer et al. 2008; Kühn et al. 2015), strongly supporting the results from Boccaletti et al. (2020). It has also been proposed that the observed inner spirals might be produced due to the interaction with an inclined and eccentric inner binary companion (Poblete et al. 2020), adding to the complexity of understanding the origin of these structures and the ongoing interactions in AB Aur.

We present two separate studies of new deep-infrared-imaging (2.2–3.7 μm) observations of AB Aurigae with the Large Binocular Telescope (LBT). The observations benefit from the unique capabilities of the LBT at these wavelengths (low background noise, pyramidal wave front sensor, real-time redundant observations) and bridge the gap between SPHERE and ALMA observations. In this study (Paper I), we focus on L'-band observations (3.7 μm) to look for the thermal emission of protoplanets and their surrounding material (circumplanetary disk and envelope; e.g., Szulágyi et al. 2019). We use both the new K_s- and L'-band LBTI images to reveal and confirm the faint disk substructures and compare them to those evidenced with SPHERE and ALMA. We present the observations and data processing in Sections 2 and 3, respectively. We set new limits on the properties of putative forming planets sculpting the circumstellar dust and gas distribution in Section 4.1. We investigate disk features in Section 4.2 and summarize the findings in Section 5.

2. Observations

Both L'- and K_s-band observations of AB Aur (A0Ve, $K = 4.23$, $L = 3.24$) were carried out at the LBT using the LBTI (Hinz et al. 2008) and its adaptive optics (AO) system, over two runs in 2014 and 2015, respectively. Data were taken using the L/M-band InfraRed Camera (LMIRCam; Skrutskie et al. 2010). All observations were performed in pupil-stabilized mode, which allows the use of angular differential imaging (ADI; Marois et al. 2006) to subtract the point-spread function (PSF) of the star to reveal its faint surroundings, particularly sharp structures and point sources. For both bands, PSF reference stars with similar brightness to AB Aur were also observed to apply reference differential imaging (RDI). This strategy can better image any extended circular and spiral structures (Milli et al. 2012) that might be expected for a system like AB Aur that is seen close to pole-on. Relevant observing parameters are given in Table 1.

2.1. L′-band Observations

L'-band ($\lambda_0 = 3.7$ μm, $\Delta\lambda = 0.58$ μm) observations of AB Aur were obtained on the nights of 2014 February 8 and February 13. On February 8, observations of AB Aur were taken only with the left (SX) side of the telescope, while both sides were used (in noninterferometric mode) on February 13. Individual exposure times were 0.175 s; five exposures were co-added within the hardware before transferring from the camera. Observations were taken at two nod positions with nodding every 1–2 minutes. On February 13, we also observed HD 39925 (K5, $K = 3.899$, $L = 3.52$) as a PSF reference star, with identical AO settings to allow for referential differential imaging (RDI). We switched between the science target and the reference twice. Because AB Aur transits within 2° of zenith at LBT, the very rapid field rotation caused the AO loop to be unstable for a few minutes. In particular, the left (SX) side AO

loop on February 13 was completely open between parallactic angles −61 to 54°. The right (DX) side obtained continuous observations in that time but with nonoptimal AO correction. Conditions varied from good seeing conditions on February 8, to poor conditions for the final acquisition of the reference star HD 39925 on February 13.

For photometric calibration, each of the saturated sequences was immediately followed by unsaturated observations of AB Aur using a neutral density filter with a transmission of 0.9%.

2.2. K_s-band Observations

K_s-band ($\lambda_0 = 2.16\ \mu$m, $\Delta\lambda = 0.32\ \mu$m) observations of AB Aur are described and analyzed in detail in Paper II (Betti et al. 2022) and used here for completeness. The observations were performed on the night of 2015 January 4, using only the left (SX) side telescope. Individual exposure times were 2 s, and observations were taken at two nod positions with nodding every 5 minutes. Two PSF reference stars, HIP 22138 (G8III, $K = 4.627$, $L = 4.582$) and HIP 24447 (K0, $K = 4.219$, $L = 4.136$), were observed before and after the observations of AB Aur, respectively, with identical instrument settings.

3. Data Reduction

3.1. Preprocessing

We employed a custom-built IDL pipeline (Bonnefoy et al. 2014) for applying bad-pixel correction, nod-subtraction, centering of the star by fitting a Moffat profile, aligning the frames, and cropping them to a 300 × 300 pixels field of view. With a plate scale of 10.7 mas px^{-1} (Maire et al. 2015), this corresponds to 3.″21×3.″21. For AB Aur, frames where the loop was open or where the AO correction was very bad were removed based on principal component analysis (PCA), with some additional bad frames not detected by this method removed manually. The PCA analysis also revealed that the PSF shape differed significantly between the two nod positions. This was attributed to the dichroic beamsplitter that sends light to both the LMIRCam and the 8–13 μm camera Nulling Optimized Mid-Infrared Camera (NOMIC) at LBTI (Hinz et al. 2016) and can cause different internal reflection and diffraction effects at different positions. We therefore treated the data from the two positions separately for the creation and subtraction of the PSF and recombined them again afterwards. The final number of usable frames in each data set is listed in Table 1.

3.2. Subtraction of the Stellar Halo

All the observations were post-processed using the IPAG-ADI pipeline (Chauvin et al. 2012). We subtracted the PSF for the data that had sufficient field rotation with closed loop through meridian transit (data sets 1 and 2 for AB Aur) using multiple ADI techniques to search for point sources and to reveal asymmetric disk structures. For those data sets where the reference star was observed immediately before or afterwards (data sets 2–7 for AB Aur), RDI processing was applied to reveal the rotationally symmetric disk structures without self-subtraction.

3.2.1. Angular Differential Imaging

We applied on data sets 1, 2, 6, and 7 classical ADI (cADI), smart ADI (sADI), radial ADI (rADI) (Chauvin et al. 2012), Locally Optimized Combination of Images (LOCI; Lafrenière et al. 2007), and Principal Component Analysis (PCA; Soummer et al. 2012) algorithms to remove the stellar halo. The use of these multiple ADI techniques allows for comparison and consistency of the results obtained at different levels of self-subtraction of the disk signal. We refer to Jorquera et al. (2021) for the configuration used for the ADI and LOCI methods. For the PCA method, observations were reduced using three different numbers of modes ($k = 1$, 5, 20), with no radial separation criteria applied for these cases.

For the L' observations of AB Aur, the parallactic angle coverage was very asymmetric, and the duration of the observations was about three times longer at parallactic angle $>+50°$ than at $<-50°$, as can be seen in Figure 4 (Appendix A). The rotation between −50 and +50° was very rapid and only a small range of parallactic angles is covered in the time before and after the rapid rotation. Constructing the PSF as the simple median of the whole cube would result in it being strongly dominated by the majority of frames taken at angles >50°. We therefore opted to use the frames at parallactic angles <0° as a reference library, to build the PSF for all frames taken at parallactic angles >0° and vice versa, using the PCA method. The relatively large average separation in time between the image and its reference PSF in this method results in suboptimal subtraction. However, it is the only way to avoid heavy self-subtraction at the location of the brightest parts of the disk. The method will essentially subtract out all flux in the image at an angle of + or −100° from the brightest region but allows us to recover regions with the most asymmetric brightness.

3.2.2. Reference Differential Imaging

For data sets 2–7, RDI substraction was performed using the PSF reference stars HD39925 (data sets 2–5), HIP 22138 (data sets 6), and HIP 24447 (data set 7). Observations were reduced using the PCA method with the same configuration as the one described in Section 3.2.1. For each data set, observations of each respective reference star were provided as a library, to derive the PSF eigenmodes used for the subtraction of the stellar contribution in the AB Aur science frames.

4. Results

Figure 1 showcases the ADI and RDI reduction of AB Aur for both L'- and K-band LBTI observations (top and bottom panels), together with a comparison with the SPHERE H-band polarimetric differential image from Boccaletti et al. (2020) (left panel). No point source appears redundantly in the various LBTI data sets (see Figure 5, Appendix B) of AB Aur at the L' band. Extended emission is however evidenced at L' in all data sets for the first time. We present the detection sensitivity inferred from the data as well as a census of the structures seen in the LBTI data below.

4.1. Search for Planetary Companions

To explore the point-source sensitivity of the LBT observations, pixel-to-pixel noise maps of each ADI reduction were estimated within a sliding box of 1.5 × 1.5 FWHM in the processed LBT field of view. We injected regularly spaced fake planets (every 10 pixels at 3 different position angles, with a flux corresponding to 100 ADU) in the original data cubes to evaluate the flux losses caused by the ADI process (e.g., Chauvin et al. 2010; Rameau et al. 2013). The final 5σ contrast

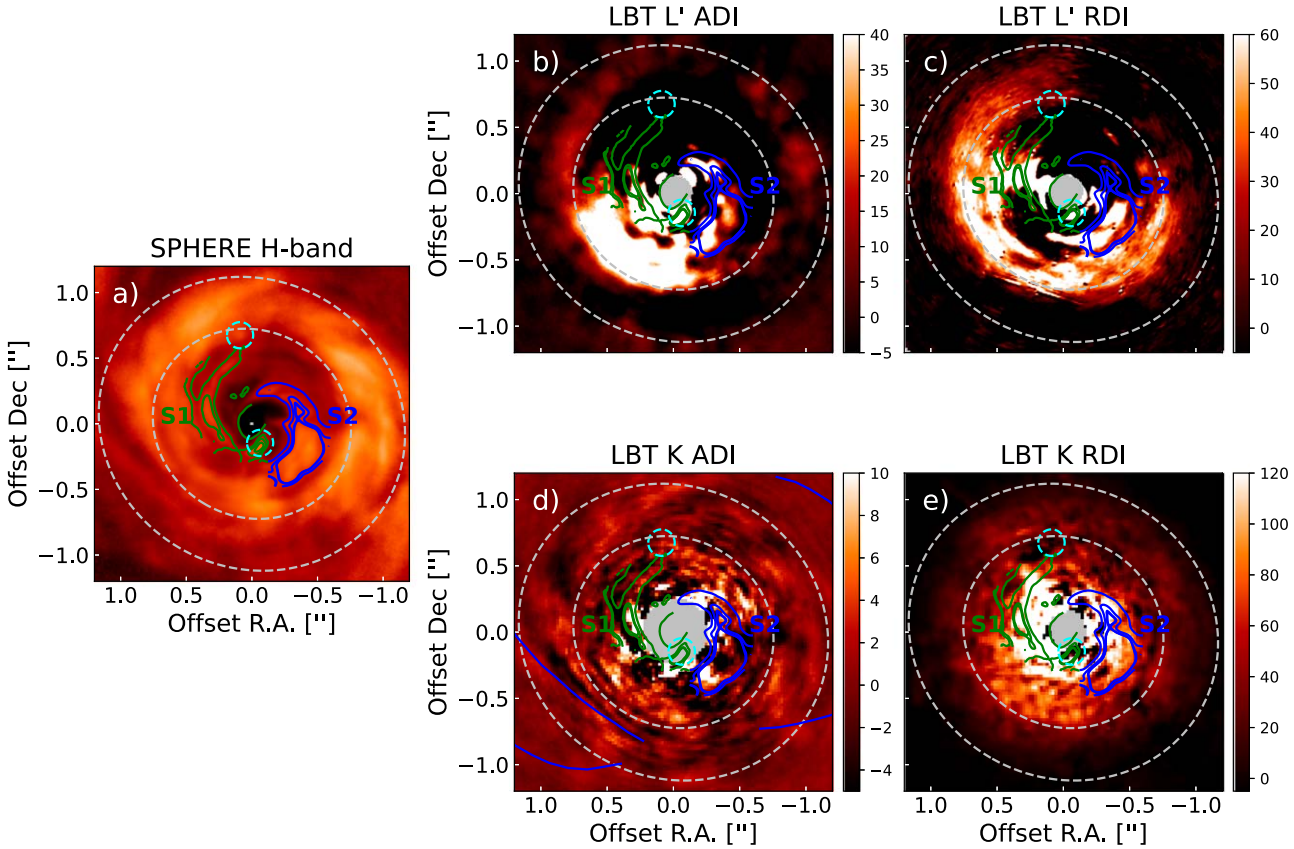

Figure 1. Comparison between ADI and RDI reductions for both the L'- (top panels) and K_s-band (bottom panels) observations of AB Aur, and the H-band polarized light image obtained with the SPHERE instrument (left panel; Boccaletti et al. 2020). Images are ordered as follows: (a) SPHERE H-band polarimetry image of AB Aur. The polarized intensity has been multiplied by the square of the stellocentric distance ($Q_{\rm phi} \times r^2$) to improve visualization of the structures. (b) Averaged LBT L'-band image from data sets 1 and 2 after ADI processing. (c) Averaged LBT L'-band image from data sets 2 to 5 after RDI processing. (d) LBT K-band image after ADI processing. (e) LBT K-band image after RDI processing. Flux is linear on all the LBT images. Dashed gray lines mark the outer ring reported by Tang et al. (2017), while the inner spiral arms of the disk reported in Tang et al. (2017) and Boccaletti et al. (2020) are denoted by solid green and blue lines. The location of the point sources identified as f1 and f2 by Boccaletti et al. (2020) are marked by a cyan dashed circle. For the case of the K-band ADI reduction, spiral features observed by Hashimoto et al. (2011) were also marked with solid blue lines in panel (d). Contrast values are given in analog-digital units (ADU) to directly showcase the results for the different reductions.

maps were obtained using the pixel-to-pixel noise maps divided by the flux loss and normalized by the relative calibration with the primary star, and were also corrected from small number statistics following the prescription of Mawet et al. (2014) to adapt our 5σ confidence level at small angles.

The detection limits for data sets 1 and 2, obtained from the cADI processing, are shown in Figure 2. On the second night, the achieved 5σ mass limits were up to 1 mag better than on the first night, depending on the separation. We reached a contrast of 10 mag at $0\farcs25$, 12.5 mag at $0\farcs5$, and 14 mag at $1''$. The 5σ contrast curves were then translated to mass limits based on the mass–luminosity relation for giant planets predicted by the ATMO 2020 (Phillips et al. 2020) and BEX-DUSTY-cold-start (Marleau et al. 2017; Asensio-Torres et al. 2021) evolutionary models. Mass limits were derived considering either a 2 and 4 Myr system. For the more optimistic scenario of 2 Myr of age, the mass limits for companions around AB Aur from the ATMO 2020 models translate to: 3–4 $M_{\rm Jup}$ beyond $0\farcs6$ (∼100 au), 6 $M_{\rm Jup}$ at $0\farcs5$ (81 au), and 14 $M_{\rm Jup}$ at $0\farcs3$ (50 au). The inner working angle of the observations is approximately $0\farcs2$ (28 au), where we would have been sensitive to brown dwarf companions with masses above $\approx$35 $M_{\rm Jup}$. In the case of the BEX-DUSTY-cold-start, models we recover a mass limit of 25–20 $M_{\rm Jup}$ between $0\farcs2$ and $0\farcs4$, 20–15 $M_{\rm Jup}$ between $0\farcs4$ and $0\farcs6$ and 15–11 $M_{\rm Jup}$ beyond $0\farcs6$. Although this results clearly indicate that we are only sensitive for high-mass objects arising from this cold-start or low entropy scenario, it is important to point out that recent works (e.g., Berardo et al. 2017; Marleau et al. 2017) have showed that cold start is actually unlikely to occur for giant planet formation and that these objects are more likely associated with a high initial entropy (Mordasini et al. 2017; Marleau et al. 2019). Because of this, further analysis regarding the possible presence of planetary companions on the system is based on our derived ATMO 2020 detection limits exclusively.

Based on our obtained mass limits, we derive a detection probability map for the second night, right-eye observations, as they provide a higher sensitivity to point sources, and assuming an age of 2 Myr. This map was obtained by using the Multi-purpose Exoplanet Simulation System code, a Monte Carlo tool for the predictions of exoplanet search results (Bonavita et al. 2012). We generated a uniform grid of masses and semimajor axis in the interval [0.5, 80] $M_{\rm Jup}$ and [10, 1000] au with a sampling of 0.5 $M_{\rm Jup}$ and 1 au, respectively. For each point in the grid, 10^4 orbits were generated with a fixed inclination and position angle (based on the inclination and position angle of the disk from Tang et al. 2017) but randomly oriented in space from uniform distributions in ω, $e < 0.1$, and M, which correspond to the argument of periastron with respect to the line of nodes, eccentricity, and mean anomaly, respectively.

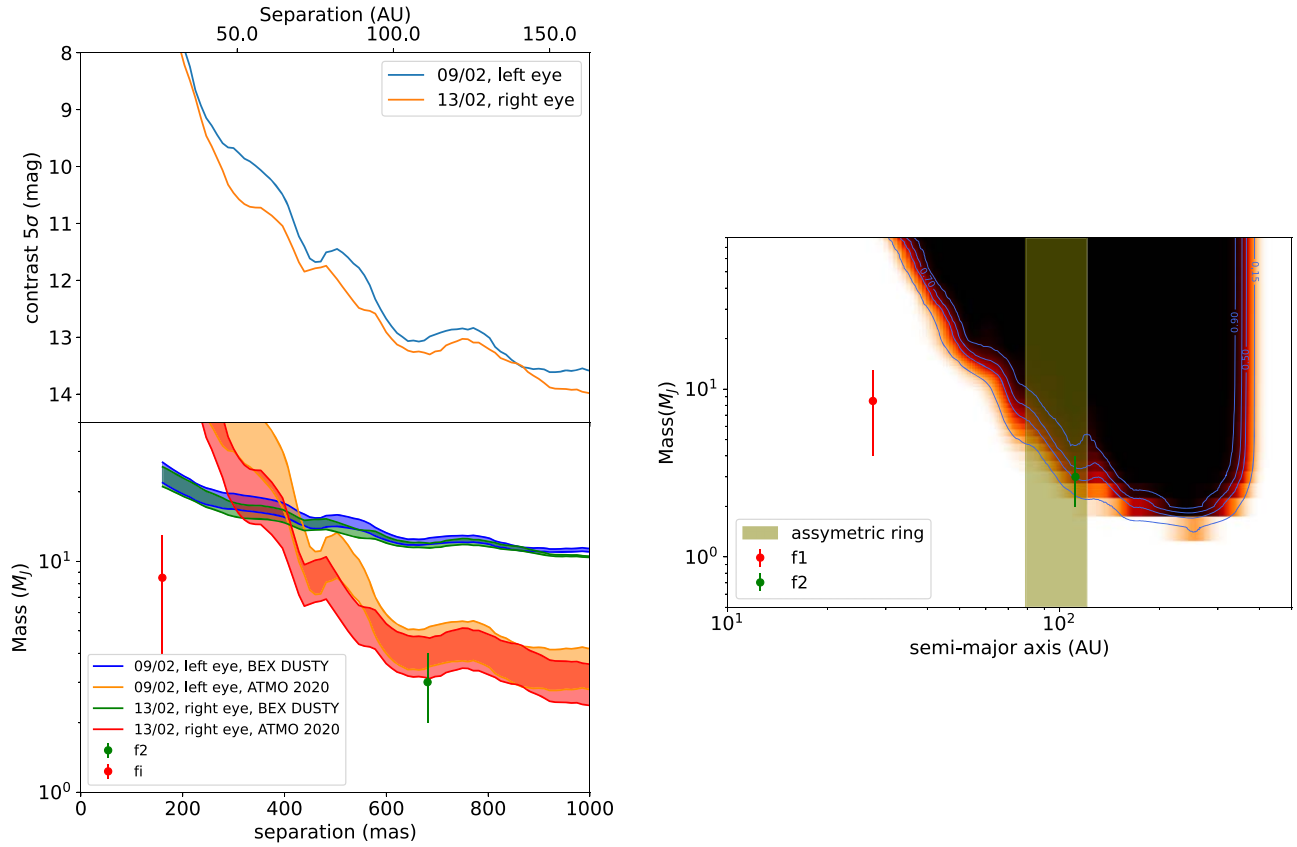

Figure 2. Top left: 5σ contrast curve achieved for the observations of AB Aur in L' taken on two different nights. Bottom left: Mass limits for point sources for the same set of observations. Shadowed regions correspond to the mass limit variation for an age between 2 Myr (lower curve) and 4 Myr (upper curve) for AB Aur, based on the ATMO 2020 and BEX-DUSTY-cold-start evolutionary models. Right: Detection probability map for AB Aur, based on the second night, right eye observations, and an age of 2 Myr for the system. The shaded green region correspond to the location and width of the asymmetric ring. The deprojected semimajor axes for f1 and f2 were derived using the inclination and position angle reported by Tang et al. (2017). The mass contrast limits are based on COND model predictions. (Baraffe et al. 2003).

The detection probability map is then built by counting the number of detected planets over the number of generated ones, by comparing the on-sky projected position (separation and position angle) of each synthetic planet with the 2D mass maps at 5σ.

Tang et al. (2017) proposed that the observed inner CO spirals might be triggered by the presence of a planetary companion at either 60–80 au or 30 au from the central star, while Boccaletti et al. (2020) recovered the signal of two apparent point sources located at a separation of 0.″16 (~26 au; f1) and 0.″681 (~111 au; f2), with f1 seemingly associated with one of the observed spirals in the H band, consistent with the predictions from the ALMA CO observations. The location and estimated masses of f1 and f2 are reported in Figures 1 and 2. None of these point sources are recovered in any of our ADI and RDI reductions at the L' and K_s bands. As we can only resolve objects down to a separation of approximately 0.″2, detection of f1 is not possible on our L' and K_s observations as is the case to the possible binary companion proposed by Poblete et al (2020). In the case of f2, the contrast derived by Boccaletti et al. (2020) is consistent with a mass ranging from 2 to 4 $M_{\rm Jup}$ based on the AMES-COND models. Boccaletti et al. (2020) also obtained a preliminary mass estimation of ~3 $M_{\rm Jup}$ based on dynamical considerations derived by Wisdom (1980), which provides a relation between location of the inner edge of the observed cavity, the star mass, and the planet's mass and distance.

This predicted mass lies in the 5σ mass limit range derived from the second night of LBTI L' observations and has a detection probability of 50% at the deprojected position of f2, for an age of 2 Myr. At first glance, this detection probability is not enough to properly confirm or discard the existence of f2. However, it is important to take into account that the derived detection probability for a given semimajor axis (orbit) does not imply that the detection probability is the same at every point of that orbit. This is because this probability is only based on the count of detected planets along the full extension of the orbit, not considering where in the orbit they were specifically recovered. We can solve this problem by looking at the bidimensional mass detection limit at the specific location of f2 (Figure 5). At this location, we obtained a 5σ mass detection limit of ~3.16 $M_{\rm Jup}$, very close to the mass limit from Boccaletti et al. (2020) obtained at shorter wavelengths (hence, likely more impacted by disk foreground extinction) and implying that the detection probability at this location should be higher than 50%. Based on these results, the lack of detection of f2 suggests it is not a real companion.

4.2. Disk Geometry and Substructures

We detect disk emission at the L' band up to ~1″ separation. The innermost extended emission (<0.″5) at the east and west sides of the disk are in good agreement with the location of the two main spirals detected by Boccaletti et al. (2020), with the

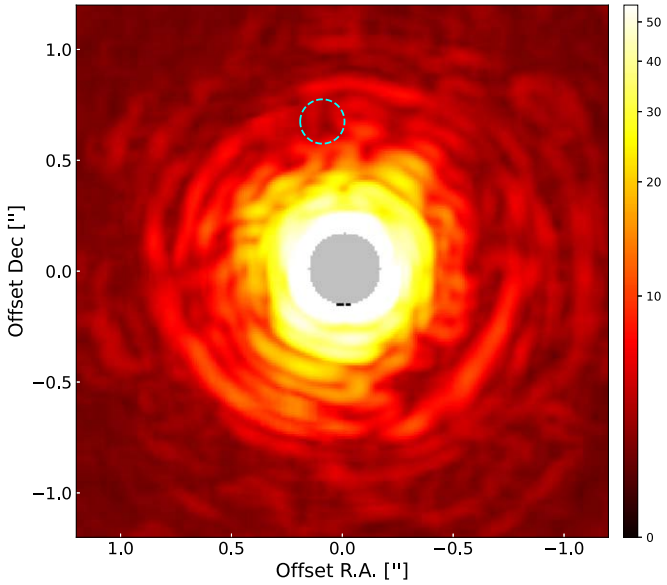

Figure 3. Mass detection map obtained for the second night of observations of AB Aur. The color bar indicates the minimum detectable mass in $M_{\rm Jup}$. The cyan circle corresponds to the location of f2.

western spiral (S2) being more clearly detected, while only the starting part of the eastern spiral (S1) appears to be recovered. The consistency of the appearance of these structures for both reduction methods (ADI and RDI), as well as for each of the independent ADI reductions (see Figure 5, Appendix B) suggests that the recovered signal effectively corresponds to the inner spirals, while the fragmented appearance of S2 is most likely caused by nonoptimal halo subtraction.

A brighter ring-like emission centered at a radius of $\approx 0\farcs56$ is evidenced in the L' and $K_{\rm s}$ LBTI images. It corresponds to a similar structure evidenced in the Subaru/HiCIAO (Hashimoto et al. 2011) and VLT/SPHERE polarized intensity H-band observations of Boccaletti et al. (2020) and shows a strong brightness asymmetry. This asymmetry is seen in the HiCIAO images but not recovered in the SPHERE observations. This suggests it to be caused by finer substructures left unresolved in our observations and Hashimoto et al. (2011) ones.

The ADI and RDI post-processed $K_{\rm s}$-band images correspond to the (d) and (e) panels of Figure 1, respectively. The inner regions ($<0\farcs5$) in the ADI images appears to be polluted by speckles. Instead, this reduction appears to be more sensitive at the outer parts of the disk, as faint emission from different structures, and particularly spirals, appears to be recovered, which is in good agreement with previously observed spirals (Hashimoto et al. 2011). Finally, the RDI reduction reveals the ring-like emission evidenced at the H and L' bands. The structure also shows the asymmetry reported at the L' band; hence it was possibly caused by the coarser angular resolution of these observations.

The ring-like structure lies at the H, $K_{\rm s}$, and L' bands within the dust ring detected in the ALMA continuum observations (1.3 mm; Tang et al. 2017) as shown in Figure 1. This difference between observed structures at different wavelengths can be explained by considering the effect of dust trapping in a disk, which can be triggered by planet-disk interactions of one or more planetary companions. The presence of a massive planet, such as the case of f1, induces a pressure enhancement on the gas distribution of the disk, which traps large particles in this pressure maxima, while smaller particles are allowed to drift into the inner cavity that is depleted of large grains (de Juan Ovelar et al. 2013; Pinilla et al. 2015; Keppler et al. 2018). This could explain why a sharp inner edge can be observed for the dust ring at 1.3 mm, which traces large particles, while dust grains of smaller size can still be detected in the cavity, producing the features observed in the NIR.

Another possible explanation for the differences in wavelength of the observed structures, specifically the asymmetric ring-like structure, arises when considering the time variability of Herbig Ae/Be stars. It has been showed that these types of systems present irregular photometric (Eiroa et al. 2002) and spectroscopic (Mendigutía et al. 2011) variations, which have been attributed to shadowing from the inner ring structure (Vioque et al. 2018; Chen et al. 2019). If that is the case for AB Aur, then it is possible that the observed differences are only product of this variability between the different epochs of observation.

Although out of the scope of this study, further modeling of the disk would allow to determine the degree asymmetry of the phase function for the dust scattering (Henyey & Greenstein 1941) and subsequently the dust grain size of the observed region, and to put strong constraints on the properties of both possible planetary companions and the protoplanetary disk, as dust trapping is heavily dependent on those parameters. At the same time, further observations at different NIR bands at similar epochs would allow to properly determine the possible time variability of AB Aur and further identify if the differences between observed structures are also influenced by these variations.

5. Conclusions

In this work, we present L'- and $K_{\rm s}$-band observations of AB Aur obtained with LBT and processed using multiple flavors of ADI and RDI methods, aimed for the detection of possible planetary companions and characterization of the disk structures, with the intention to bridge the results obtained from SPHERE NIR and ALMA submillimeter observations of the same target. Our main results can be summarized as follows.

1. No planetary companions were detected in our observations. Contrast (5σ magnitude) and mass detection limits were derived from the L' observations of the target, serving as a first estimator for the detectability of planetary companions in the system. Our results translate to 3–4 $M_{\rm Jup}$ beyond $0\farcs6$ up to 14 $M_{\rm Jup}$ at $0\farcs3$ (50 au). Comparison with previous estimations on the location of possible companions at $0\farcs16$ (26 au; f1) and $0\farcs681$ (111 au; f2) reveal that f1 cannot be resolved in our observations, based on the degradation of the ADI and RDI methods at this separation. In the case of f2, we set an upper mass limit of 3.16 $M_{\rm Jup}$ for a nonextincted massive planet based on our L' detection limits.
2. Part of the spiral structures resolved in both CO and polarimetric H-band observations at the inner region ($<0\farcs5$) of the disk were recovered from the L' observations, although poorly resolved due to the performance of the ADI and RDI methods at this separations and wavelengths with LBT.
3. We report the first detection of the ring structure of the system at L', which shows a brightness asymmetry also noticed in HiCIAO H and the LBTI $K_{\rm s}$-band observations but not in the SPHERE H-band data. This apparent

inconsistency might be cause by the different angular resolution of the various ground-based observations.

4. We discuss dust trapping in the disk and time variability of Herbig Ae/Be stars as the possible explanation for the difference in asymmetry observed between the different bands. Further observations and modeling are needed to properly determine the effect that each of these phenomena have in the observed structures.
5. The ADI reduction K_s-band observations also allows to resolve the outer structures of the disk, revealing the presence of spiral arms, which are in very good agreement with previously observed spiral structures.

The L'-band images of AB Aur add to the limited sample of disks resolved at these wavelengths from the ground (e.g., Currie et al. 2019; Wagner et al. 2019, 2020; Wang et al. 2020). Such challenging observations should increase steadily with the recent L'-band imagers operating on 8 m class telescopes fed by adaptive-optics systems, better adapted to the observations of red dust-enshrouded host stars (LBT/LMIRCam, Keck/NIRC2, VLT/ERIS-NIX).

S.J. acknowledges support from the National Agency for Research and Development (ANID), Scholarship Program, Doctorado Becas Nacionales/2020-21212356. EB was supported by the Swiss National Science Foundation (SNSF). L.P. gratefully acknowledges support by the ANID BASAL projects ACE210002 and FB210003, and by ANID,—Millennium Science Initiative Program—NCN19_171. This research has made use of the SIMBAD database, operated at CDS, Strasbourg, France, and of NASA's Astrophysics Data System Bibliographic Services. This work benefited from the support of the project FRAME ANR-20-CE31-0012 of the French National Research Agency (ANR).

Appendix A
Parallactic Angle Variation

In Figure 4 we present the parallactic angle coverage for the seven independent sets of observations of AB Aur.

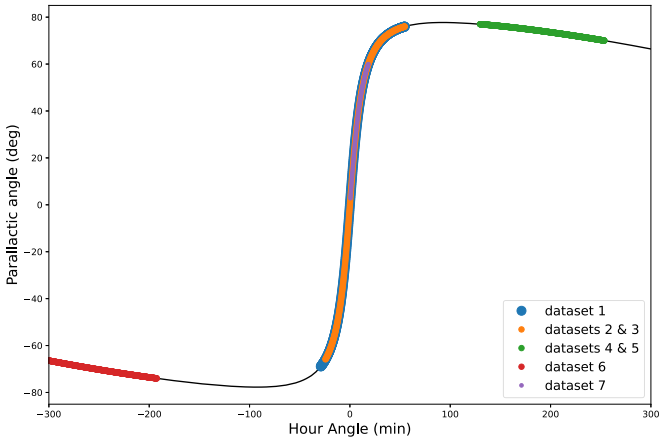

Figure 4. Parallactic angle variation of the seven independent data sets of observations of AB Aur. The black line indicates the expected variation of the parallactic of the object during a normal night, taking into account the rotation of the FOV due to the use of the pupil-stabilized mode.

Appendix B
ADI Reduction

Figure 5 showcases the ADI reduction for data sets 1 and 2, with the observations before and after the meridian passage, reduced separately for each case. This allows to check for consistency on the recovered structures and to discard possible artifacts. In all cases, we recover part of the inner spirals S1 and S2, as well as the bright part of the disk on the southeast region.

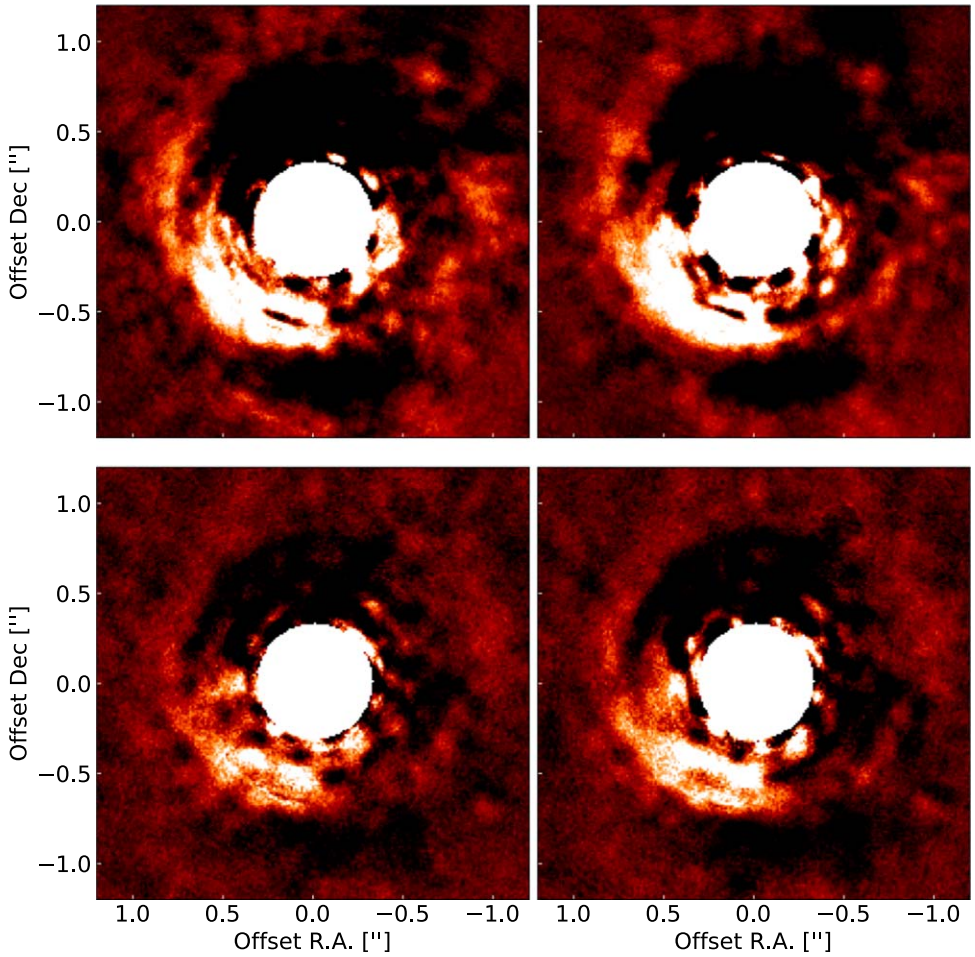

Figure 5. Top: ADI reduction from AB Aur observations obtained using the left side of the telescope. Bottom: ADI reduction from AB Aur observations obtained using the right side of the telescope. Left (Right) images were constructed using observations before (after) the meridian passage.

ORCID iDs

Sebastián Jorquera https://orcid.org/0000-0001-6822-7664
Mickaël Bonnefoy https://orcid.org/0000-0001-5579-5339
Sarah Betti https://orcid.org/0000-0002-8667-6428
Gaël Chauvin https://orcid.org/0000-0003-4022-8598
Esther Buenzli https://orcid.org/0000-0003-3306-1486
Laura M. Pérez https://orcid.org/0000-0002-1199-9564
Katherine B. Follette https://orcid.org/0000-0002-7821-0695
Philip M. Hinz https://orcid.org/0000-0002-1954-4564
Anthony Boccaletti https://orcid.org/0000-0001-9353-2724
Vanessa Bailey https://orcid.org/0000-0002-5407-2806
Beth Biller https://orcid.org/0000-0003-4614-7035
Denis Defrère https://orcid.org/0000-0003-3499-2506
Josh Eisner https://orcid.org/0000-0002-1031-4199
Thomas Henning https://orcid.org/0000-0002-1493-300X
Hubert Klahr https://orcid.org/0000-0002-8227-5467
Jarron Leisenring https://orcid.org/0000-0002-0834-6140
Johan Olofsson https://orcid.org/0000-0003-4475-3605
Joshua E. Schlieder https://orcid.org/0000-0001-5347-7062
Andrew J. Skemer https://orcid.org/0000-0001-6098-3924
Michael F. Skrutskie https://orcid.org/0000-0001-8671-5901
Roy Van Boekel https://orcid.org/0000-0002-2190-3108

References

ALMA Partnership, Brogan, C. L., Pérez, L. M., et al. 2015, ApJL, 808, L3
Andrews, S. M., Huang, J., Pérez, L. M., et al. 2018, ApJL, 869, L41
Asensio-Torres, R., Henning, T., Cantalloube, F., et al. 2021, A&A, 652, A101
Avenhaus, H., Quanz, S. P., Garufi, A., et al. 2018, ApJ, 863, 44
Baraffe, I., Chabrier, G., Barman, T. S., Allard, F., & Hauschildt, P. H. 2003, A&A, 402, 701
Benisty, M., Bae, J., Facchini, S., et al. 2021, ApJL, 916, L2
Benisty, M., Juhasz, A., Boccaletti, A., et al. 2015, A&A, 578, L6
Berardo, D., Cumming, A., & Marleau, G.-D. 2017, ApJ, 834, 149
Betti, S. K., Follette, K., & Jorquera, S. 2022, arXiv:2201.08868
Boccaletti, A., Di Folco, E., Pantin, E., et al. 2020, A&A, 637, L5
Bonavita, M., Chauvin, G., Desidera, S., et al. 2012, A&A, 537, A67
Bonnefoy, M., Currie, T., Marleau, G. D., et al. 2014, A&A, 562, A111
Chauvin, G., Lagrange, A. M., Beust, H., et al. 2012, A&A, 542, A41
Chauvin, G., Lagrange, A. M., Bonavita, M., et al. 2010, A&A, 509, A52
Chen, L., Moór, A., Kreplin, A., et al. 2019, ApJL, 887, L32
Currie, T., Marois, C., Cieza, L., et al. 2019, ApJL, 877, L3
de Juan Ovelar, M., Min, M., Dominik, C., et al. 2013, A&A, 560, A111
DeWarf, L. E., Sepinsky, J. F., Guinan, E. F., Ribas, I., & Nadalin, I. 2003, ApJ, 590, 357
Eiroa, C., Oudmaijer, R. D., Davies, J. K., et al. 2002, A&A, 384, 1038
Fukagawa, M., Hayashi, M., Tamura, M., et al. 2004, ApJL, 605, L53
Gaia Collaboration, Brown, A. G. A., Vallenari, A., et al. 2018, A&A, 616, A1
Hashimoto, J., Tamura, M., Muto, T., et al. 2011, ApJL, 729, L17
Henyey, L. G., & Greenstein, J. L. 1941, ApJ, 93, 70
Hinz, P. M., Bippert-Plymate, T., Breuninger, A., et al. 2008, Proc. SPIE, 7013, 701328
Hinz, P. M., Defrère, D., Skemer, A., et al. 2016, Proc. SPIE, 9907, 990704
Jorquera, S., Pérez, L. M., Chauvin, G., et al. 2021, AJ, 161, 146
Keppler, M., Benisty, M., Müller, A., et al. 2018, A&A, 617, A44
Kühn, J., Mennesson, B., Liewer, K., et al. 2015, ApJ, 800, 55
Lafrenière, D., Marois, C., Doyon, R., Nadeau, D., & Artigau, É. 2007, ApJ, 660, 770
Maire, A. L., Skemer, A. J., Hinz, P. M., et al. 2015, A&A, 579, C2
Marleau, G.-D., Klahr, H., Kuiper, R., & Mordasini, C. 2017, ApJ, 836, 221
Marleau, G.-D., Mordasini, C., & Kuiper, R. 2019, ApJ, 881, 144
Marois, C., Lafrenière, D., Doyon, R., Macintosh, B., & Nadeau, D. 2006, ApJ, 641, 556
Mawet, D., Milli, J., Wahhaj, Z., et al. 2014, ApJ, 792, 97
Mendigutía, I., Eiroa, C., Montesinos, B., et al. 2011, A&A, 529, A34
Millan-Gabet, R., Monnier, J. D., Berger, J. P., et al. 2006, ApJL, 645, L77
Milli, J., Mouillet, D., Lagrange, A. M., et al. 2012, A&A, 545, A111
Mordasini, C., Marleau, G. D., & Mollière, P. 2017, A&A, 608, A72
Oppenheimer, B. R., Brenner, D., Hinkley, S., et al. 2008, ApJ, 679, 1574
Pérez, S., Casassus, S., Hales, A., et al. 2020, ApJL, 889, L24
Perrin, M. D., Schneider, G., Duchene, G., et al. 2009, ApJL, 707, L132
Phillips, M. W., Tremblin, P., Baraffe, I., et al. 2020, A&A, 637, A38
Piétu, V., Guilloteau, S., & Dutrey, A. 2005, A&A, 443, 945
Pinilla, P., de Juan Ovelar, M., Ataiee, S., et al. 2015, A&A, 573, A9
Pinte, C., Price, D. J., Ménard, F., et al. 2020, ApJL, 890, L9
Pinte, C., van der Plas, G., Ménard, F., et al. 2019, NatAs, 3, 1109
Poblete, P. P., Calcino, J., Cuello, N., et al. 2020, MNRAS, 496, 2362
Rameau, J., Chauvin, G., Lagrange, A. M., et al. 2013, A&A, 553, A60
Skrutskie, M. F., Jones, T., Hinz, P., et al. 2010, Proc. SPIE, 7735, 77353H
Soummer, R., Pueyo, L., & Larkin, J. 2012, ApJL, 755, L28
Stolker, T., Dominik, C., Avenhaus, H., et al. 2016, A&A, 595, A113
Szulágyi, J., Dullemond, C. P., Pohl, A., & Quanz, S. P. 2019, MNRAS, 487, 1248
Tang, Y.-W., Guilloteau, S., Dutrey, A., et al. 2017, ApJ, 840, 32
Tang, Y. W., Guilloteau, S., Piétu, V., et al. 2012, A&A, 547, A84
Uyama, T., Currie, T., Christiaens, V., et al. 2020, ApJ, 900, 135
Vioque, M., Oudmaijer, R. D., Baines, D., Mendigutía, I., & Pérez-Martínez, R. 2018, A&A, 620, A128
Wagner, K., Stone, J., Dong, R., et al. 2020, AJ, 159, 252
Wagner, K., Stone, J. M., Spalding, E., et al. 2019, ApJ, 882, 20
Wang, J. J., Ginzburg, S., Ren, B., et al. 2020, AJ, 159, 263
Wisdom, J. 1980, AJ, 85, 1122